Sarah K. Patch, PhD

k-Space Data Preprocessing for Artifact Reduction in MR Imaging[1]

Fourier transforms are ubiquitous in nature; magnetic resonance (MR) imaging is just one of many examples. Music is perhaps the best-known example. Standard scores represent pitch in the Fourier, or frequency, domain but leave duration in the time domain (Fig 1). If we were to Fourier transform with respect to time, the results would be a two-dimensional (2D) frequency × frequency representation—the direct analog to 2D k-space!

To a first-order approximation, MR imagers measure the Fourier transform of the density of (typically hydrogen) nuclei. This assumption is, strictly speaking, false (1), but clinical imagers are often within just a few "parts per million" of sampling the true Fourier transform. In MR lingo, Fourier space is often referred to as k-space, and we use the terms interchangeably. The imaging chain consists of many small steps grouped into four main steps: acquisition, preprocessing, reconstruction, and postprocessing. The data acquisition step collects information particular to that patient. Preprocessing steps apply a priori information to correct or modify the measured patient data, making the data more consistent with MR physics and reconstruction theory. Subsequent steps merely modify and, at best, preserve the combination of patient data and a priori information. Therefore, it is critical that each step be accurate in order to generate diagnostic images and renderings.

Computed tomographic (CT) systems sample Radon data, which can be directly related to MR imaging data. We begin by exploring the differences between MR and CT imaging data—and the differences in final reconstructed images. Large errors, such as those created by gradient nonlinearity that result in image warping, are typically corrected by means of postprocessing (2,3). For most non-Cartesian MR images, data preprocessing consists of resampling measured data onto a Cartesian lattice suitable for inversion via fast Fourier transform (FFT).

This chapter gives a brief—and by no means exhaustive—overview of different MR imaging techniques and their data preprocessing requirements. Currently, the lion's share of clinical images sample Fourier space on a Cartesian lattice that is immediately invertible via FFT, as depicted in Figure 2. We start by examining artifacts suffered by all MR images. Gibbs ringing is the result of sampling over only a finite

RSNA2005
Connecting for
Lifelong Learning

region of k-space; k-space apodization (smoothing) reduces ringing artifacts. We then consider spiral scanning, one of several non-Cartesian data acquisition schemes, and examine the process by which data sampled on a non-Cartesian set of points are resampled onto a Cartesian set suitable for FFT. Why this process works especially well for MR imaging data and how it can fail are discussed. Finally, we consider PROPELLER (periodically rotated overlapping parallel lines with enhanced reconstruction), a relatively new hybrid technique (4–7). PROPELLER fills Fourier space by sampling multiple rotated Cartesian data sets using fast spin-echo MR imaging, a standard (ie, slow) acquisition scheme, as depicted in Figure 3. The effective temporal resolution of PROPELLER is improved by exploiting relationships among the redundant measurements to minimize motion artifacts.

DIFFERENCES BETWEEN CT AND MR IMAGING DATA

CT scanners measure (essentially) the Radon transform with great accuracy, whereas MR imagers sample the Fourier transform. Although these transforms are directly related via the projection slice theorem, their properties are drastically different, resulting in important differences in image quality. Although one could spend a semester studying the fine points of these transforms, most of the essentials are captured in a simple example.

In Figure 4, we compare the raw and filtered CT data of a simple disk with the analogous MR imaging data. Notice that the raw Radon projections are continuous but have "corners." High-pass filtering coarsens CT data prior to backprojection, particularly at the corners. This sharply contrasts with the MR k-space data, which are extremely smooth and always have the largest variations in the center of k-space.

CT scanners must always resample data onto data points required for image reconstruction. Most MR pulse sequences are designed to sample data at exactly the Cartesian lattice points required for image reconstruction via FFT. Non-Cartesian k-space trajectories, such as spirals and PROPELLER, permit higher temporal resolution and/or correction for patient motion, respectively, and require resampling the data onto a Cartesian lattice.

The interpolation, or "gridding," of CT data therefore suffers the greatest errors around the edges of the object, whereas MR imaging gridding errors are largest in the center of k-space. This difference results in drastically different types of artifacts in reconstructed images, as depicted in Figures 4 and 5. CT scans tend to suffer streaks and Gibbs ringing off high-contrast objects, whereas MR images frequently suffer low-frequency shading due to interpolation errors in the center of k-space. The k-space data are the Fourier transform
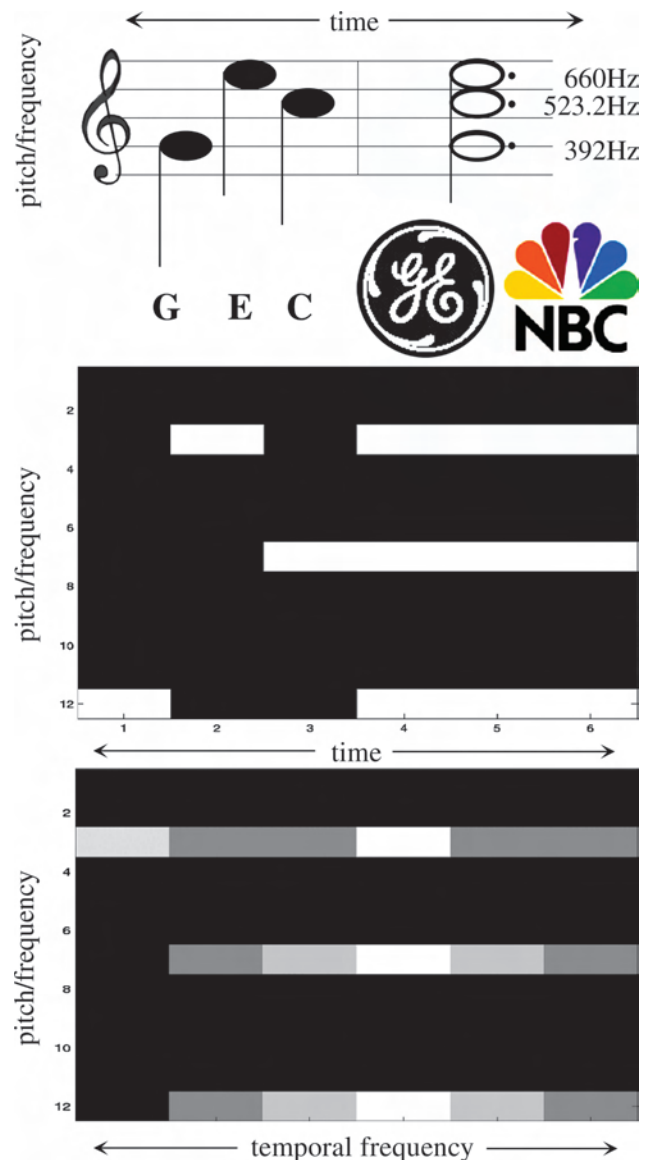
Figure 1. Top: Musical score represents the NBC jingle in pitch-time. Note that pitch is in units of frequency (Hz). Middle: Same jingle represented as a 2D pitch-time image. Bottom: Representation in pitch-frequency domain. For simplicity, only magnitude is displayed.

of the imaging function f. We use the notation $\mathrm{F}f(k)$ for k-space data and $f(x)$ for the reconstructed image.

APODIZATION

Even MR pulse sequences that sample data on Cartesian lattice points at the Nyquist rate result in imperfect images. This unfortunate fact is related to Heisenberg's uncertainty principle: A function cannot be both space and band limited (8). The patient occupies only a finite region in space, so the imaging object is space limited. This means that its Fourier transform (ie, measured k-space data) has infinite support. By sampling over only a finite region of k-space, we abruptly cut off high-frequency information. This is equivalent to multiplying the infinite-
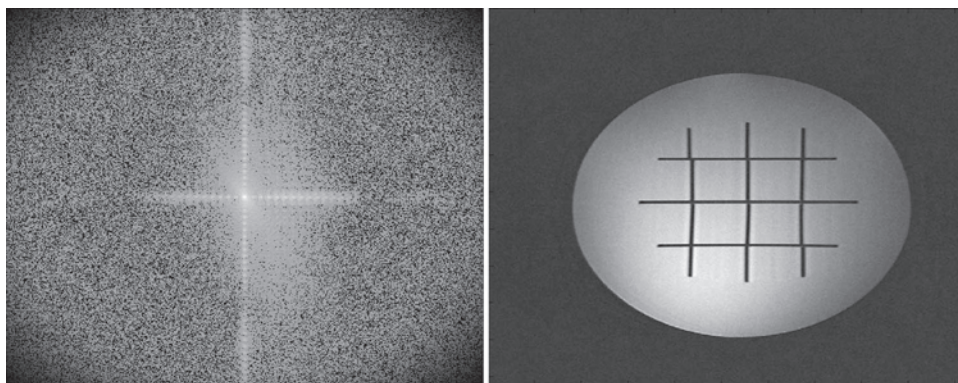
Figure 2. Left: Apodized k-space data sampled on an evenly spaced Cartesian lattice permits immediate inversion via FFT. Log of k-space magnitude data is displayed. Right: Reconstructed image. The image's checkerboard pattern corresponds to strong signal along the x and y axes in k-space.
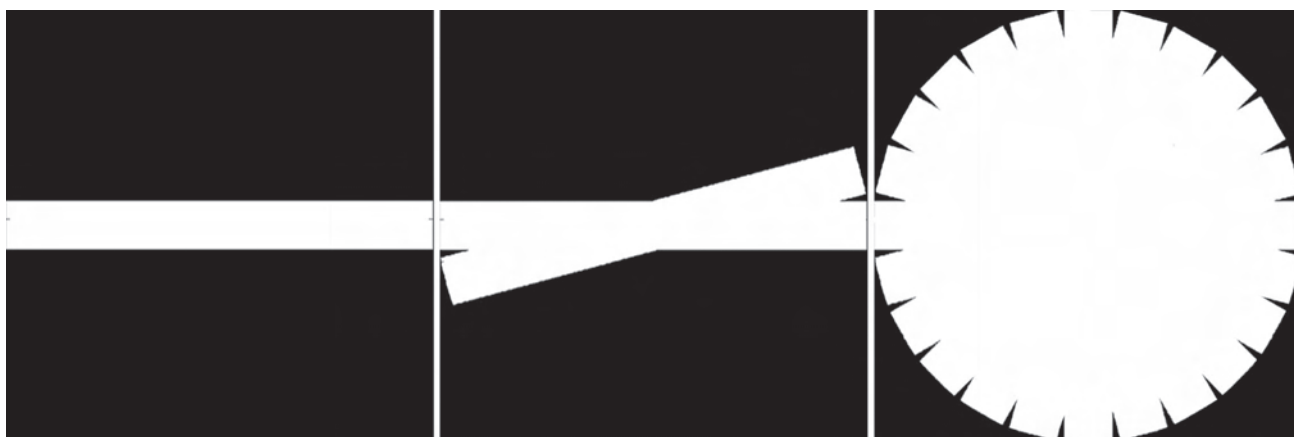

Figure 3. PROPELLER fills in k-space by acquiring rotated Cartesian data sets, typically with a fast spin-echo pulse sequence. Left: Blade 1 fills in a horizontal rectangle throughout k-space. Middle: Blade 2 measures the same low-frequency information as blade 1 but different high-frequency information. Right: Most of k-space is sampled by one of 12 blades.

support k-space data by an indicator function, I, that is identically 1 on the sampling region and 0 outside, effectively convolving the image with an approximate delta function. We mention the most important aspects of convolutions below and then delve into their effect on image quality.

CONVOLUTION

Convolving two functions is essentially a "shift-and-sum" procedure. For each point, x, at which we want to evaluate the convolution of two functions f and e, we first shift the function $e(-\gamma)$ by x, multiply with the unshifted f, and then integrate to "sum up" the result:

$$(f *e)(x) = \int f(\gamma)\, e(x-\gamma)\, d\gamma. \qquad (1)$$

This is depicted in Figure 6. Notice that convolving a function against a delta function yields the very same function:

$$(f *\delta)(x) = \int f(\gamma)\, \delta(x-\gamma)\, d\gamma = f(x). \qquad (2)$$

Another fundamental property of convolutions that has a dramatic effect on MR image reconstruction is

the fact that the Fourier transform of a convolution is the product of Fourier transforms,

$$\mathrm{F}(f *e)(k) = \mathrm{F} f(k)\, \mathrm{F} e(k), \qquad (3)$$

and, conversely,

$$\mathrm{F}^{-1}(\mathrm{F} f *\mathrm{F} e)(x) = f(x)\, e(x). \qquad (4)$$

GIBBS RINGING

When MR data are simply reconstructed by FFT of the measured data, the reconstructed image suffers Gibbs ringing near sharp discontinuities, as shown in Figures 4 and 7. Such artifacts are removed by convolving the image with a smoothing function δ_{smooth}, or multiplying the k-space data by $\mathrm{F}\delta_{smooth}$. One choice for apodization is the Tukey window, shown in Figure 8 (9).

SPIRALS

Spiral scanning is faster than conventional Cartesian scanning for two reasons. First, spirals naturally collect
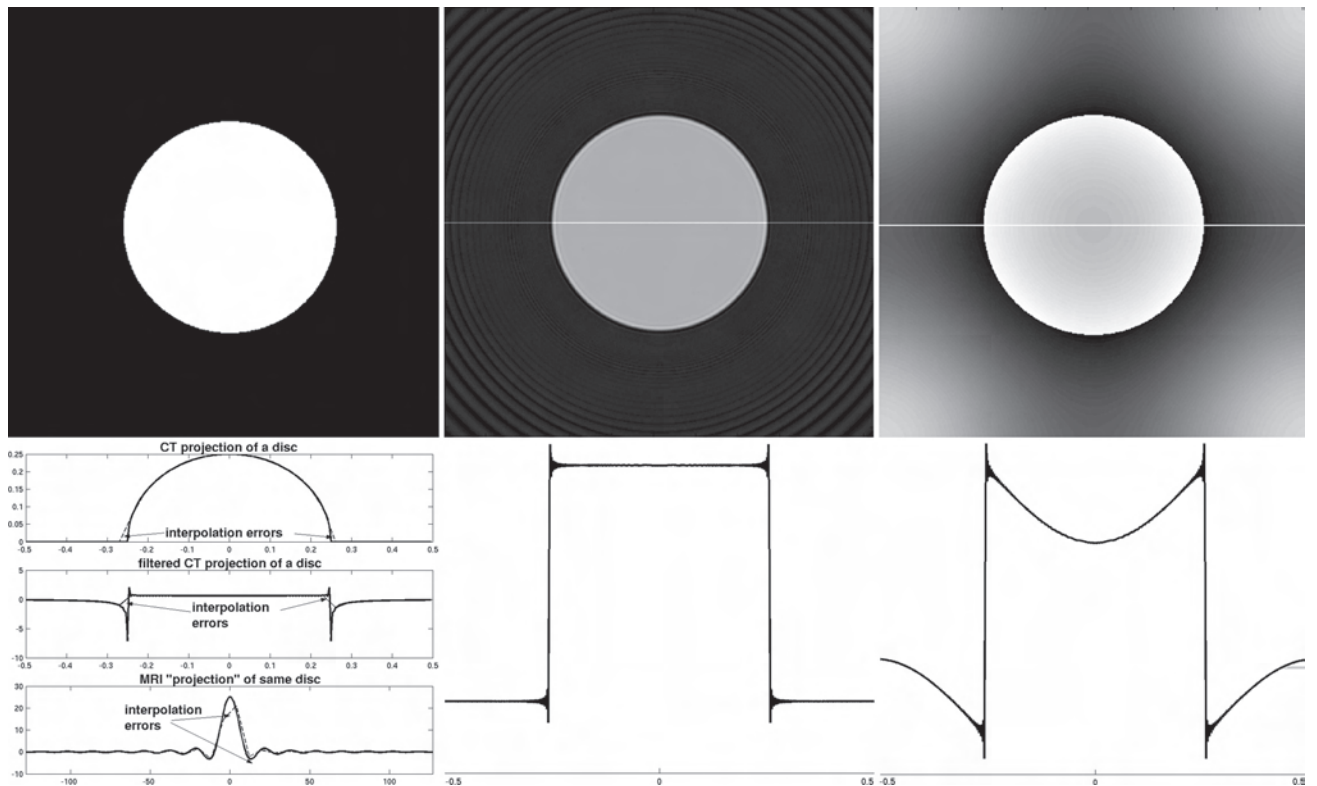
Figure 4. Top left: Original disk. Top middle: CT reconstruction. Top right: MR imaging reconstruction with exaggerated gridding errors in the center of k-space. Bottom left: CT projection, filtered CT projection, and MR imaging (MRI) k-space projection. Bottom middle: Profile through CT reconstruction. CT reconstruction suffers artifacts due to Gibbs ringing and interpolation errors. Bottom right: Profile through MR imaging reconstruction. MR imaging reconstruction suffers Gibbs ringing as well as low-frequency shading due to interpolation errors in k-space.

Figure 5. MR PROPELLER images (top) and spiral CT images (bottom). Top left: Gridding errors result in low-frequency shading across the MR image. Top right: Gridding is deconvolved to improve contrast. Bottom left: High-order interpolation between CT detectors results in streaks off bone (arrows). Bottom right: Apodized interpolation reduces streaking. (Reprinted, with permission, from reference 15.)
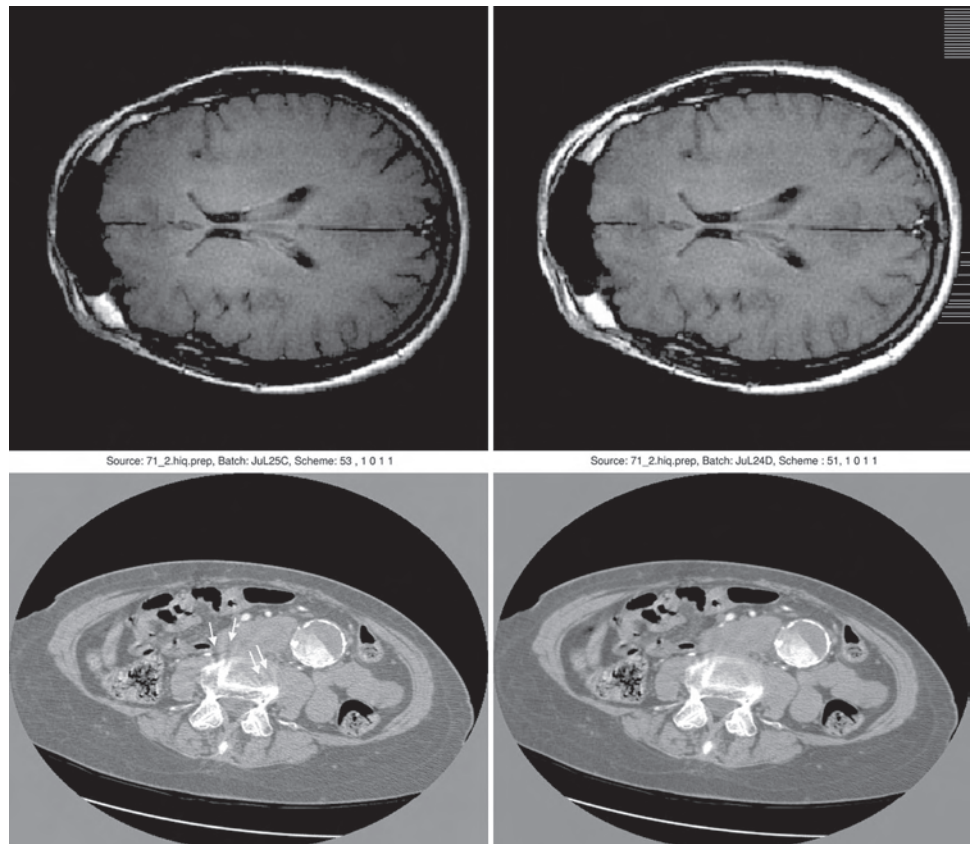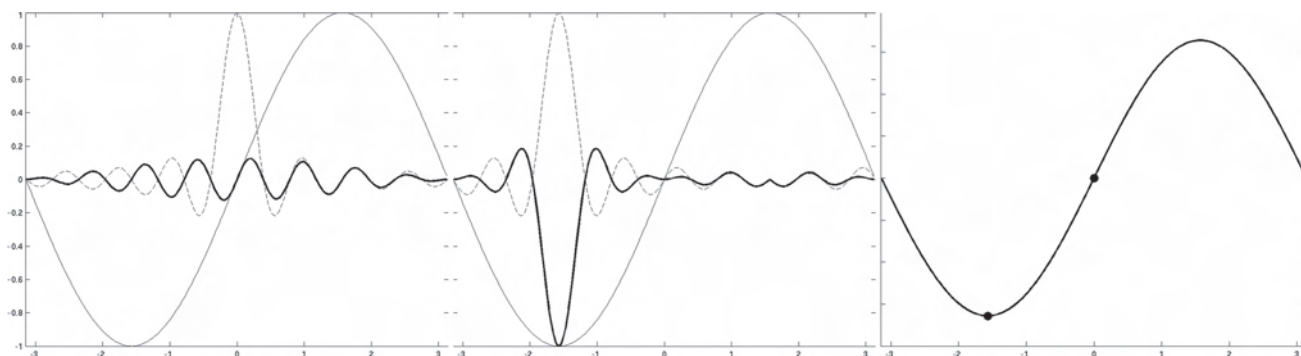
Figure 6. Convolution over the interval $(-\pi, \pi)$ of sinc$(16x) = \text{sinc}_{16}(x)$ with $\sin(x)$; (sinc$_{16}$ * sin)(x) is computed by multiplying sinc$(x-16y)$ pointwise against $\sin(y)$ and integrating the result. Left: (sinc$_{16}$ * sin)$(0) = \int \text{sinc}(0-16y) \sin y \, dy$; dashed line is sinc$(0-16y)$; solid thin line is sinc$_{16}(y)$; and thick black line is sinc$(-16y)\sin(y)$. Middle: (sinc$_{16}$ * sin)$(-\pi/2) = \int \text{sinc}(-\pi/2-16y) \sin y \, dy$; dashed line is sinc$(-\pi/2-16y)$; solid thin line is $\sin(y)$; and thick black line is sinc$(-\pi/2-16y)\sin(y)$. Right: (sinc$_{16}$ * sin)(x) evaluated throughout the interval $(-\pi, \pi)$. Dots denote values of (sinc$_{16}$*sin)$(-\pi/2)$ and (sinc$_{16}$*sin)(0).
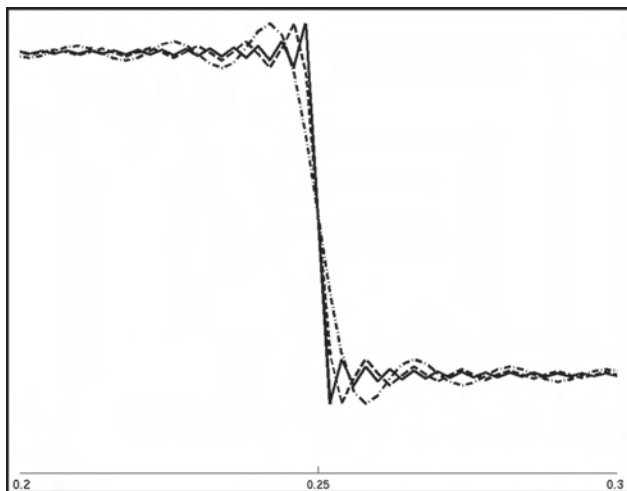

Figure 7. Gibbs ringing shown near the edge of the disk seen in Figure 4. Solid line is k-space data sampled on 512 × 512 grid; dashed line is on 128 × 128 grid; and dashed-dotted line is on 64 × 64 grid.

only the circular center of k-space, reducing the sampling area by a factor of $(4-\pi)/4 \sim 1/4$ (see Fig 9). Second, spiral scans take far better advantage of hardware limits and therefore travel through k-space faster than most Cartesian acquisitions.

The costs of improved temporal resolution in spiral scanning include the following:

1. Resampling, or "gridding," the measured data from spiral trajectories onto a Cartesian lattice.

2. Gross trajectory errors due to field inhomogeneity. The image quality effects are far more benign in Cartesian scans than in spirals, as depicted in Figures 9 and 10.

3. Blurring due to off-resonance effects.

Because it is fundamental to all non-Cartesian pulse sequences, we focus on gridding in the following section and simply mention that high-order data corrections may also improve spiral image quality.

GRIDDING

"Gridding" is MR imaging lingo for data resampling or data fitting. Interpolation is simply one form of gridding. There is a slew of literature on gridding techniques, in many scientific fields besides MR imaging (10–14). As depicted in Figure 4, gridding of k-space data is far more forgiving than gridding of CT data. Furthermore, MR data tend to contain more random noise than CT sinograms. Most non-Cartesian MR data sets are therefore gridded by convolving against a severely space-limited kernel.

The first implication of gridding convolution is that when data happen to already be sampled on a Cartesian lattice, we can easily—and accurately—sinc interpolate onto another Cartesian lattice by taking FFTs. This is done on a PROPELLER blade in Figure 11. The second implication for non-Cartesian data acquisitions is that when gridding, we convolve the measured data against an approximate delta function, F$e(\mathbf{k})$, so the reconstructed image is therefore multiplied by $e(\mathbf{x})$. In other words, gridding smooths k-space data, introducing low-frequency shading in image space.

Interpolation is a form of gridding, and we will examine linear interpolation in one dimension before moving on to sinc and jinc interpolation. Finally, we will consider interpolation kernels that are currently used in clinical MR imaging systems.

Linear Interpolation

Linear interpolation in one dimension is the simplest form of gridding, in which data are estimated at desired sample points by evaluating the function obtained by drawing straight line segments between the measured data points, as shown in Figure 12. This is equivalent to convolving measured data with the tent function, which is the convolution of an indicator with itself:

Figure 8. Tukey window function with cutoff $\mathbf{k}_c = 108$ and roll-off window of $w = 20$. Left: Window function in k-space. Right: Point spread function in image space. (Reprinted, with permission, from reference 16.)
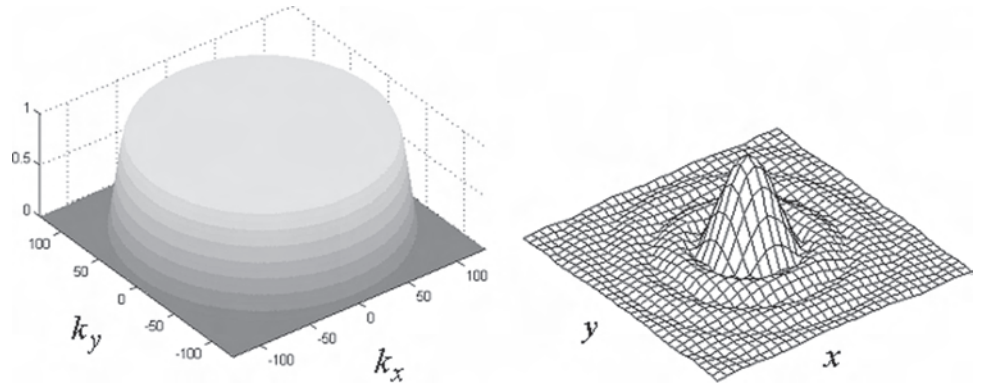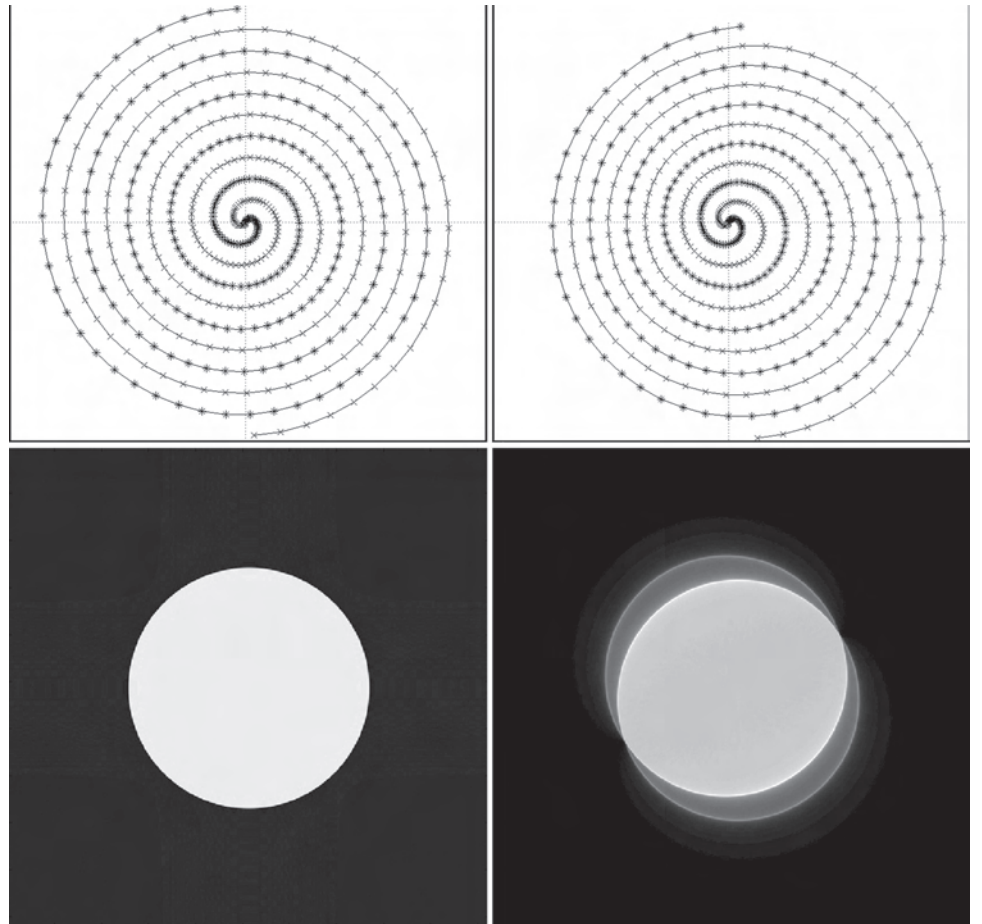

Figure 9. Simulations to show effect of field inhomogeneity on spiral MR imaging. Top left: Spiral trajectories as designed. Top right: Spiral trajectories drift when pushed by a linear gradient in the background magnetic field. Bottom left: Uniform disk reconstructed from ideal spiral data. Bottom right: Reconstruction from distorted spiral measurements.

$$\mathrm{F}f_{\mathrm{lin}}(k) = \frac{[(k-k_i)\mathrm{F}f(k_{i+1})+(k_{i+1}-k)\,\mathrm{F}f(k_i)]}{(k_{i+1}-k_i)}$$
$$= [\mathrm{F}f *^d \Lambda](k)$$
$$= [\mathrm{F}f *^d (I*I)](k), \tag{5}$$

where $*$ denotes standard, or continuous, convolution, $*^d$ denotes discrete convolution, Λ denotes the tent function, and I denotes the indicator function. Linear interpolation in k-space smooths the k-space data, resulting in low-frequency shading across the image, because convolution in k-space corresponds to

multiplication in image space:

$$f_{\mathrm{lin}}(x) = f(x)\,\mathrm{sinc}^2(x). \tag{6}$$

This effect is depicted in Figure 12 and is discussed in detail in the "Gridding Deconvolution" section later in this chapter. To avoid aliasing, we typically interpolate onto a Cartesian lattice with a smaller step size than the original sampling step size, creating a reconstructed image with a larger field of view (FOV). This pushes many artifacts out of the desired FOV, as depicted in Figure 11.
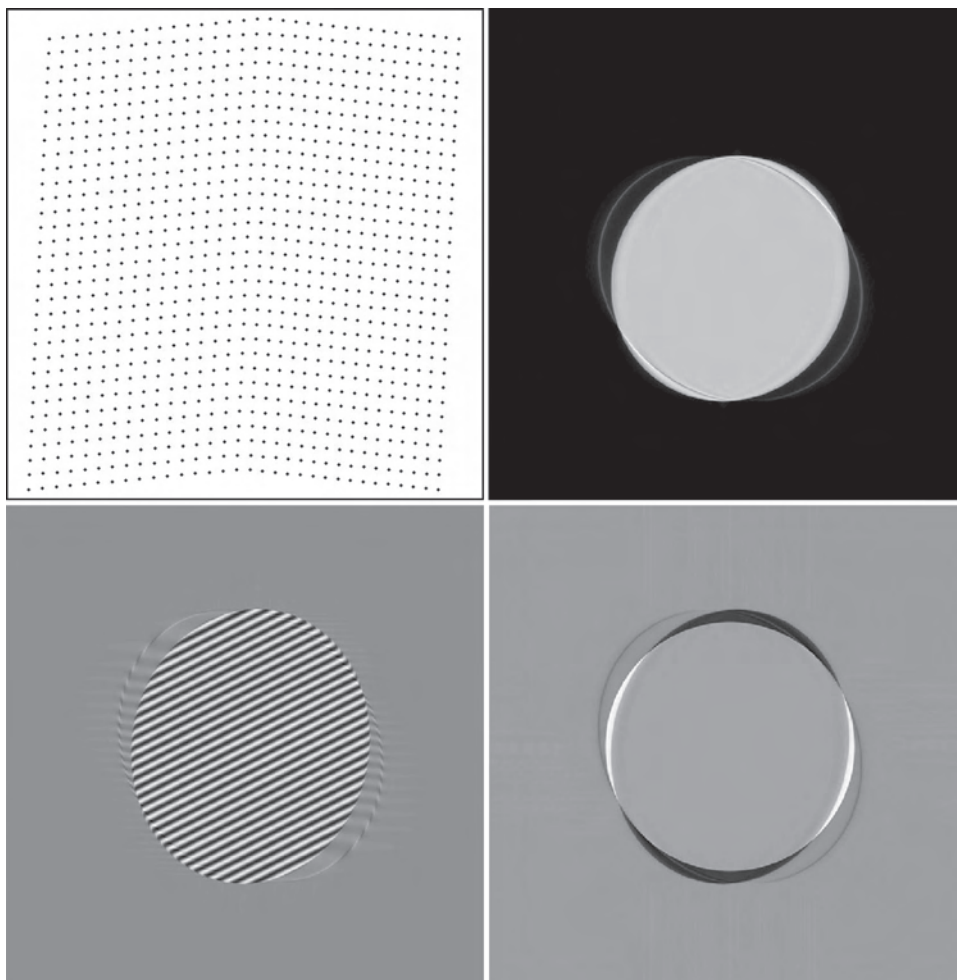
Figure 10. Simulations show that Cartesian acquisitions are more robust to field inhomogeneity. Top left: Field inhomogeneity translates and distorts k-space sampling more coherently than in spiral scans. Top right: Magnitude image suffers fewer artifacts than spiral, despite severe phase roll (bottom left). Bottom right: Image distortion displayed in difference image between magnitude images with and without field inhomogeneity.
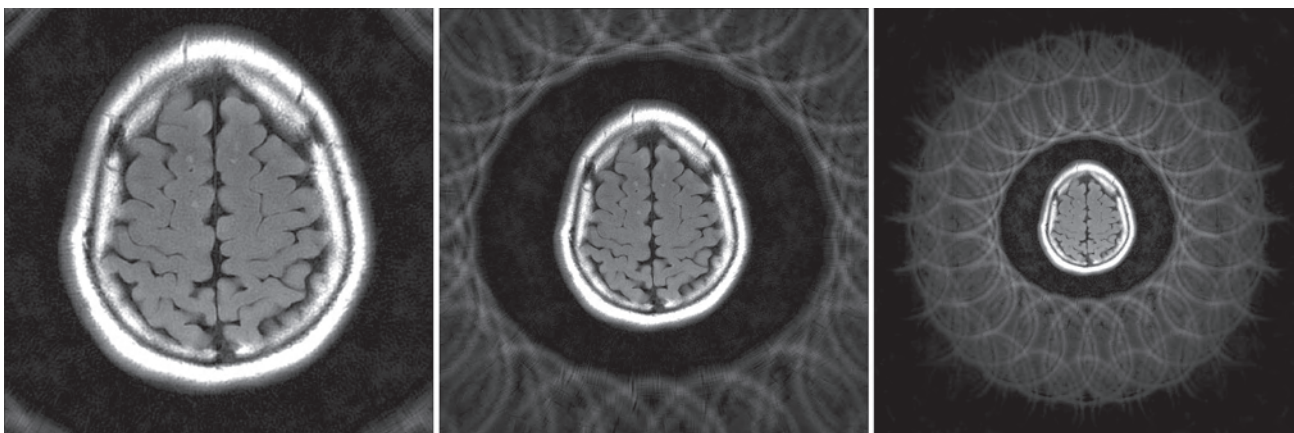

Figure 11. PROPELLER MR image is regridded onto a Cartesian lattice that increases the FOV by a factor of up to four in each direction. Left: Image at the desired FOV. Middle: Cropped image at two times the desired FOV shows severe ringing artifacts pushed outside the FOV. Right: A second ring of aliasing artifacts is barely visible in a $4\times$ FOV.

Sinc Interpolation

The ideal situation is to choose a gridding technique that causes no shading across the image. Because we typically grid onto a more finely discretized lattice that increases the FOV, the "ideal" interpolator is convolution with the Fourier transform of the indicator function over the desired FOV. In other words, ideal interpolation is convolution of measured data against the Fourier transform of the function that is identically 1 inside the desired FOV and is zero outside. These functions are

Figure 12. Top left: "Tent" function by which k-space data are convolved during linear interpolation. Top right: Image shading due to interpolation. No interpolation causes no shading, as denoted by solid line. Linear interpolation onto a finer k-space lattice with one-quarter of the spacing creates a reconstructed image over four times the FOV, with shading denoted by dashed line. Higher-order cubic interpolation creates a reconstructed image with shading denoted by dashed-dotted line. Bottom left: k-Space data sampled at x's and linearly interpolated onto points designated by dots. Bottom right: Ideal image, without interpolation (solid line). Four-times-FOV image from data interpolated with linear and cubic interpolation (dashed and dashed-dotted lines, respectively) suffers severe shading.
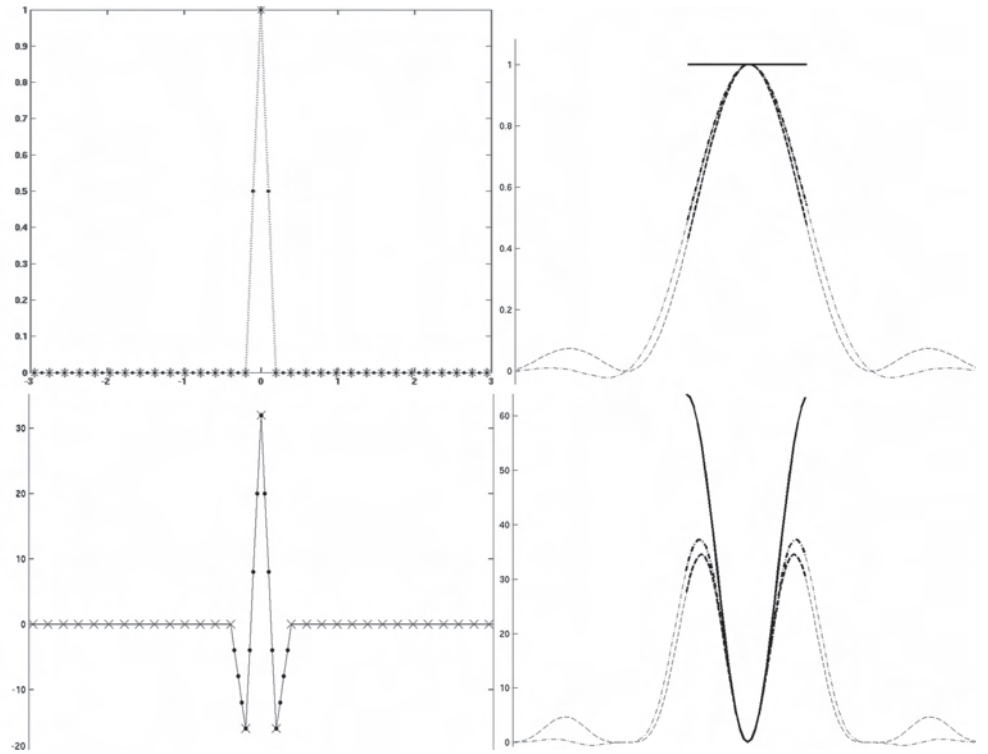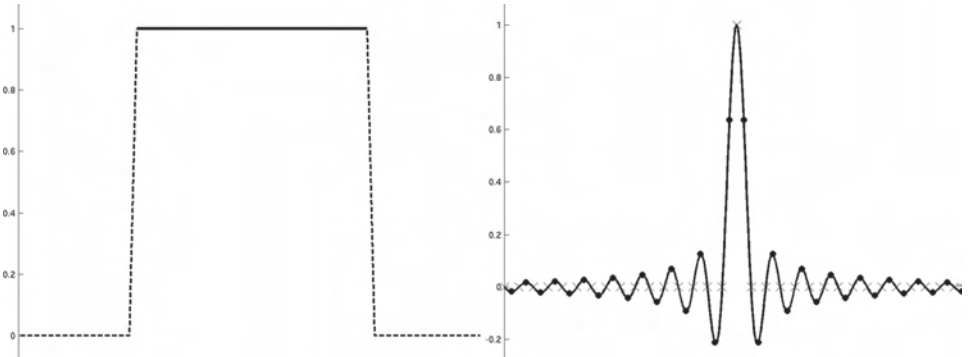
Figure 13. Left: Ideal image shading, where image FOV is doubled to prevent aliasing artifacts. Right: Sinc interpolator, which when convolved with measured data puts exactly the data values back onto sampled points, because the sinc is a Kronecker delta function when evaluated only at the x's.

called "sinc" functions and have the form, sinc $(x) = \sin x / x$. Suppose the final reconstructed FOV is $4L$; then ideal interpolation is discrete convolution of k-space data with a sinc function evaluated at lattice points, as shown in Figure 13:

$$
\begin{aligned}
f_{\text{ideal}}(x) &= [fI](x) = \mathrm{F}^{-1}(\mathrm{F}f *^{d}\mathrm{F}I)(x) \\
&= \mathrm{F}^{-1}(\mathrm{F}f *^{d}\text{sinc})(x).
\end{aligned}
\tag{7}
$$

So far, we have considered interpolation in one dimension. The concepts are easily extended to two dimensions, either by taking tensor products or by extending to radial functions. An example of tensor product sinc interpolation is shown in Figure 14. We examine the perfect 2D radial interpolator next.

Jinc Interpolation

MR imaging requires gridding data in 2D—or sometimes 3D—k-space. For head images, the patient's head

is contained within the head coil and cannot occupy corners of a full-FOV image, so the ideal interpolator may be the Fourier transform of an indicator on a disk. The Fourier transform of a radial function is radial, so in this case we convolve with a radial function, as depicted in Figure 15:

$$
\begin{aligned}
f_{\text{ideal}}(\mathbf{x}) &= [fI_{|\mathbf{x}|^2 < 1/4}](\mathbf{x}) \\
&= \mathrm{F}^{-1}([\mathrm{F}f *^{d}\mathrm{F}I_{|\mathbf{x}|^2 < 1/4}])(\mathbf{x}) \\
&= \mathrm{F}^{-1}\left[\mathrm{F}f *^{d}\left(\frac{2J_1(\pi|\mathbf{k}|)}{\pi|\mathbf{k}|}\right)\right](\mathbf{x}),
\end{aligned}
\tag{8}
$$

where $(x,y) = \mathbf{x}$. The trouble with sinc and jinc interpolation is that although both produce great image quality, both are computationally costly because convolution kernels have support throughout all of k-space, as shown in Figures 13 and 15. Convolving with a kernel that has "small" support reduces
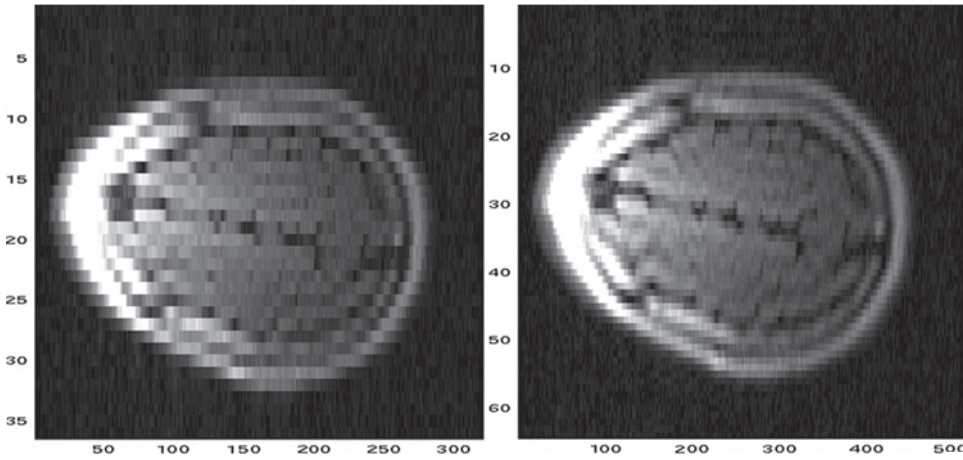
Figure 14. Left: MR image from a single phase-corrected PRO-PELLER blade with an echo train length of 36 and a readout length of 320. Right: MR image sinc interpolated up to 64 × 512.
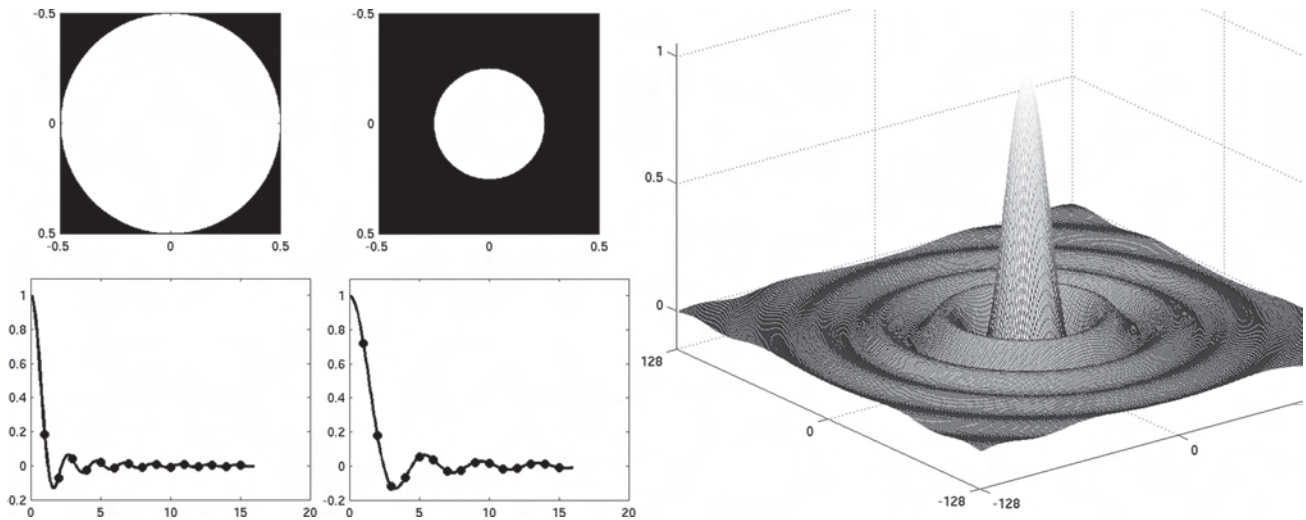

Figure 15. Perfect radial interpolation requires convolution of k-space data by the Fourier transform of an indicator function on the disk. Top left: Disk of radius FOV/2. Bottom left: Plot of jinc(*r*). Top middle: Disk of radius FOV/4. Bottom middle: Plot of jinc(*r*/2). Right: Jinc ideal radial convolution kernel.

Formula	Projection Reconstruction	Archimedes Spiral
Trajectory and Density Compensation Formulas for Projection Reconstruction and Archimedes Spiral Acquisitions		
k-Space point	$\boldsymbol{K}(t, \theta) = te^{i\theta}$	$\boldsymbol{K}(\theta, \text{shot})$ $= \theta(t)e^{i(\theta+2\pi\,\text{shot}/N\,\text{shots})}$
$\triangle\boldsymbol{K}$, density compensation	$\triangle\boldsymbol{K}(t, \theta) = t$	$\triangle\boldsymbol{K}(\theta, \text{shot})$ $= (\theta\,d\theta/dt)(t)$

gridding time, and if the kernel is carefully chosen, image quality is largely preserved (see Figure 16).

Density Compensation

Convolution of discretely sampled data is written as a sum,

$$(f * e)(x) = \sum_j f(\gamma_j)e(x - \gamma_j)\Delta\gamma_j, \qquad (9)$$

where the sum runs over all sample points γ_j such that $(x - \gamma_j)$ lies inside the support of e, and $\Delta\gamma_j$ is the discrete analog of $d\gamma$, running roughly inversely proportional to sampling density. For simple non-Cartesian trajectories such as projection reconstruction and Archimedes spirals, the sampling density can be calculated analytically, as listed in the Table and depicted in Figure 17. For more complicated k-space trajectories, the density compensation may require numerical calculation.

Deconvolution

Equation (4) implies that any gridding scheme multiplies the true image by the Fourier transform of the gridding kernel. This can be seen in the one-dimensional example presented in Figure 12. Typically, gridding kernels are approximate delta functions, so their Fourier transforms are slowly varying functions introducing low-frequency shading across the reconstructed image. Dividing the reconstructed image by

81

Figure 16. Left column: Jinc interpolation with only kernel points within **k** < FOV/16. Right column: "Perfect" jinc interpolation provides a minor improvement over a compactly supported kernel. Top: Reconstructed MR images. Middle: Convolution kernels. Only the nonzero portion of the fast(er) kernel with small support is displayed. Bottom: Fourier transforms of convolution kernels. Reconstructed image = true image × F(ker).
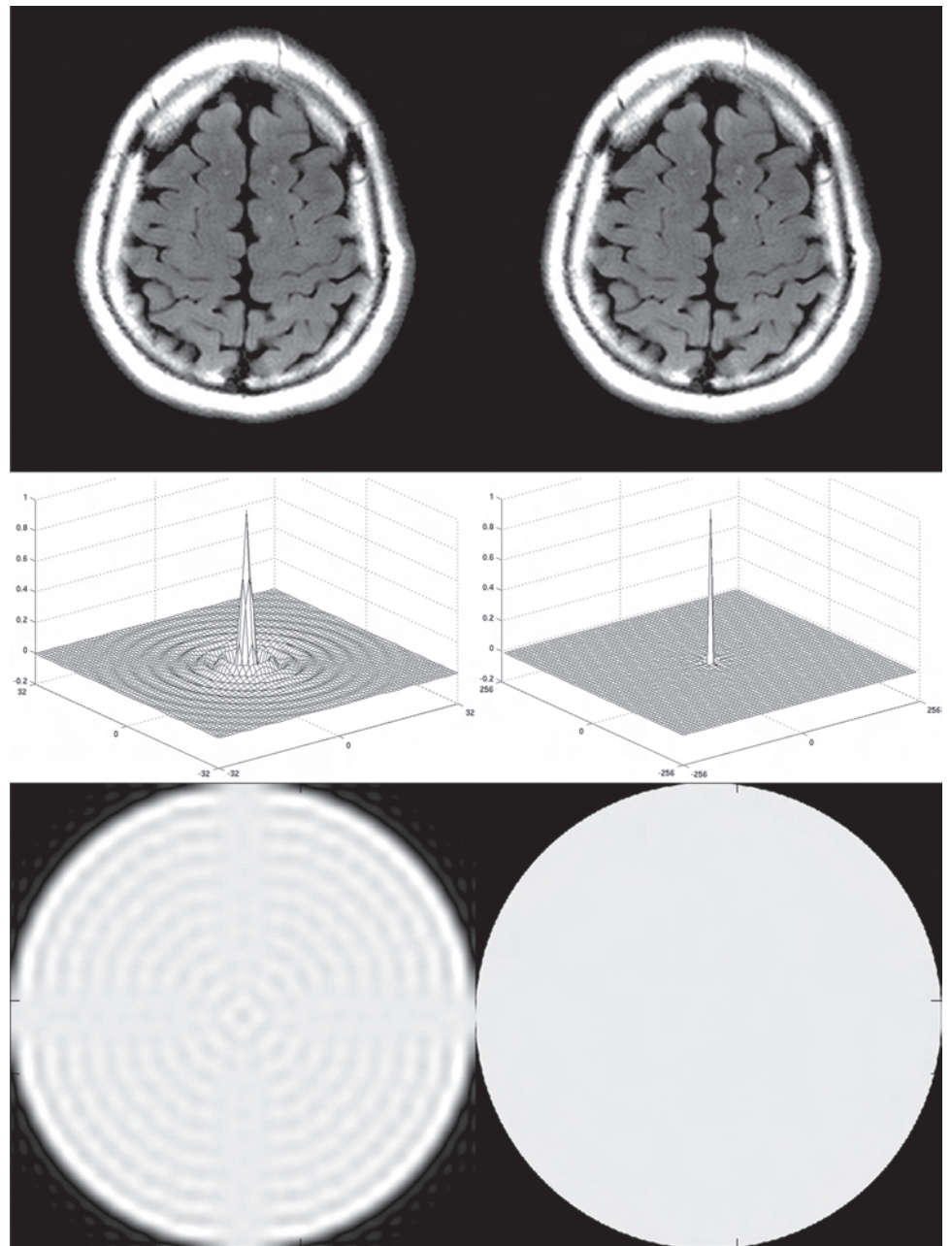
the Fourier transform of the gridding kernel deconvolves the gridding kernel, improving low-contrast detectability, as shown in Figure 5 (top).

PROPELLER

From an image reconstruction point of view, PROPELLER can be thought of as an extension of projection reconstruction imaging. PROPELLER is a relatively new hybrid technique that fills in k-space by sampling multiple rotated Cartesian data sets by using a standard (ie, slow) acquisition scheme, as depicted in Figure 3. In the limit as the blade width approaches one k-space line, PROPELLER turns into projection reconstruction. However, for blade widths

much greater than one k-space readout line, PROPELLER samples redundant data in the center of k-space, permitting several data corrections. Indeed, reconstruction of PROPELLER data requires far more data correction steps than most other MR imaging data sets.

Correction steps include the following:

1. Phase correction, which refocuses each echo and makes each blade's image nearly real. It also serves to recenter blades that may not have been exactly centered in the middle of k-space.

2. Rotation correction, which corrects for in-plane patient rotation.

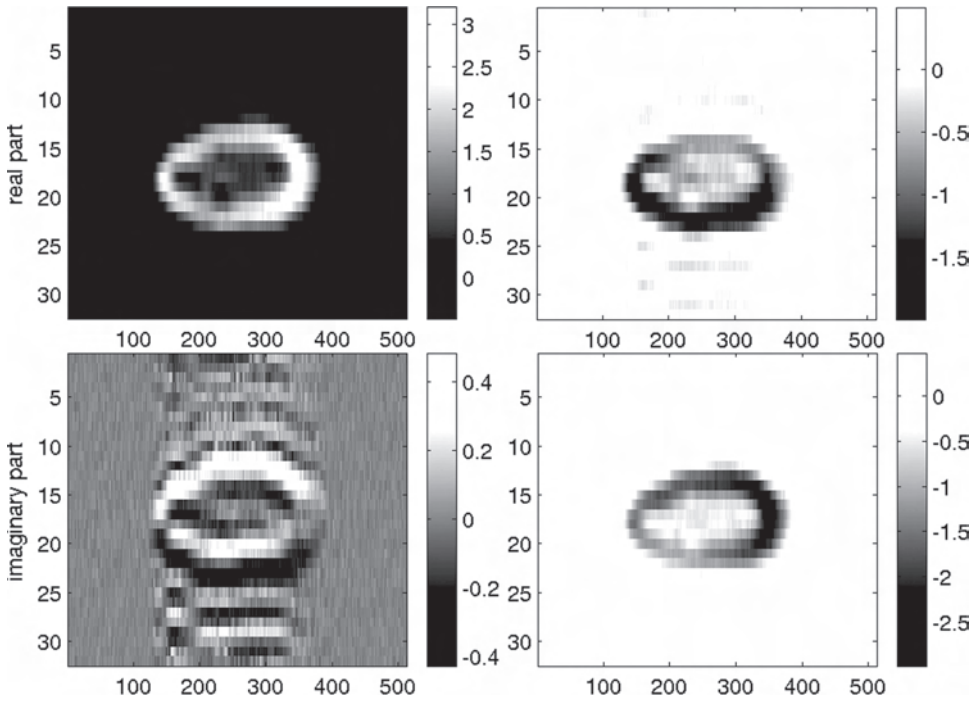3. Shift correction, which corrects for in-plane patient translation.

Figure 18. Top left: Real part of phase-corrected blade image. Top right: Real part of image from raw blade. Bottom left: Imaginary part of phase-corrected blade image. Bottom right: Imaginary part of image from raw blade. Note scale difference; phase-corrected blade is essentially real.
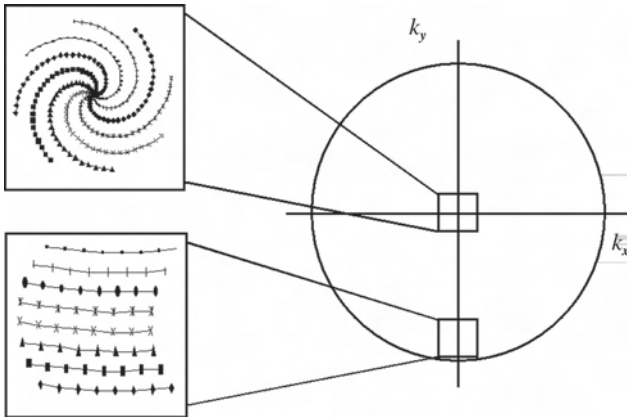

Figure 17. Archimedes spirals sample low frequencies far more densely than the Nyquist rate. (Reprinted, with permission, from reference 16.)

4. Data correlation, which correlates low-frequency data across blades and then assigns low priority to blades with low correlation values.

5. Density correction, for regridding onto a single Cartesian lattice.

6. Gridding onto a single Cartesian lattice.

Finally, the image is reconstructed via FFT, and gridding is deconvolved. The six preprocessing steps are detailed in the following sections.

Phase Correction

Blades are combined to fill in k-space for final reconstruction, so errors that vary from blade to blade must be eliminated. For instance, eddy currents may be different for different blade orientations, the patient may move between blade acquisitions, and so on. This first data correction step serves to refocus the echo within each blade, ensuring that each blade is centered in k-space. Low-frequency phase rolls are essentially removed from each blade image, making k-space blades essentially Hermitian symmetric (4). This is done in the image domain. Each blade is transformed into image space by means of FFT. A low-pass filtered version of the same blade is also subjected to FFT, creating a low-frequency blade image. The phase of the low-pass image is removed from the full-bandwidth blade image, which is subsequently returned to k-space by means of inverse FFT, as follows:

$$w(k_x, k_y) = \Lambda(k_x)\Lambda(k_y), \tag{10}$$

so

$$\mathrm{F}^{-1}w(x, y) = \mathrm{sinc}^2(x)\,\mathrm{sinc}^2(y), \tag{11}$$

$$\begin{aligned} f_{\mathrm{win}}(x, y) &= \mathrm{F}^{-1}[(\mathrm{F}f)w](x, y) \\ &= |f_{\mathrm{win}}(x, y)|e^{i\phi_{\mathrm{win}}(x, y)} \end{aligned}, \tag{12}$$

$$f_{\mathrm{corr}}(k_x, k_y) = \mathrm{F}[fe^{-i\phi_{\mathrm{win}}}](k_x, k_y). \tag{13}$$

Pre- and postcorrection blade images are shown in Figure 18.

Rotation Correction

Rigid body motion of an object affects its Fourier transform in a well-behaved fashion. Rotation of an object rotates its Fourier transform,

Figure 19. Three-bottle phantom images from a 23-blade acquisition. Brightest circle is from a bottle filled with vegetable oil. Other bottles contain solutions designed to simulate white and gray matter. White matter: NiCl$_2$, 1.532 mmol/L, with 1.09% agarose gel and 0.1% potassium sorbate (percentages by weight). Gray matter: NiCl$_2$, 0.904 mmol/L, with 0.95% agarose gel. Top: Phantom positioned on left (left image) and right (right image) sides of the FOV. Bottom: Blades 1:12 from first data set combined with blades 13:23 from second data set to simulate motion during imaging. Reconstructions are shown without (left) and with (right) motion correction. Correlation correction yields drastically different values, as shown in Figure 20. Remaining artifacts are primarily due to errors in estimating positions for blade 1.
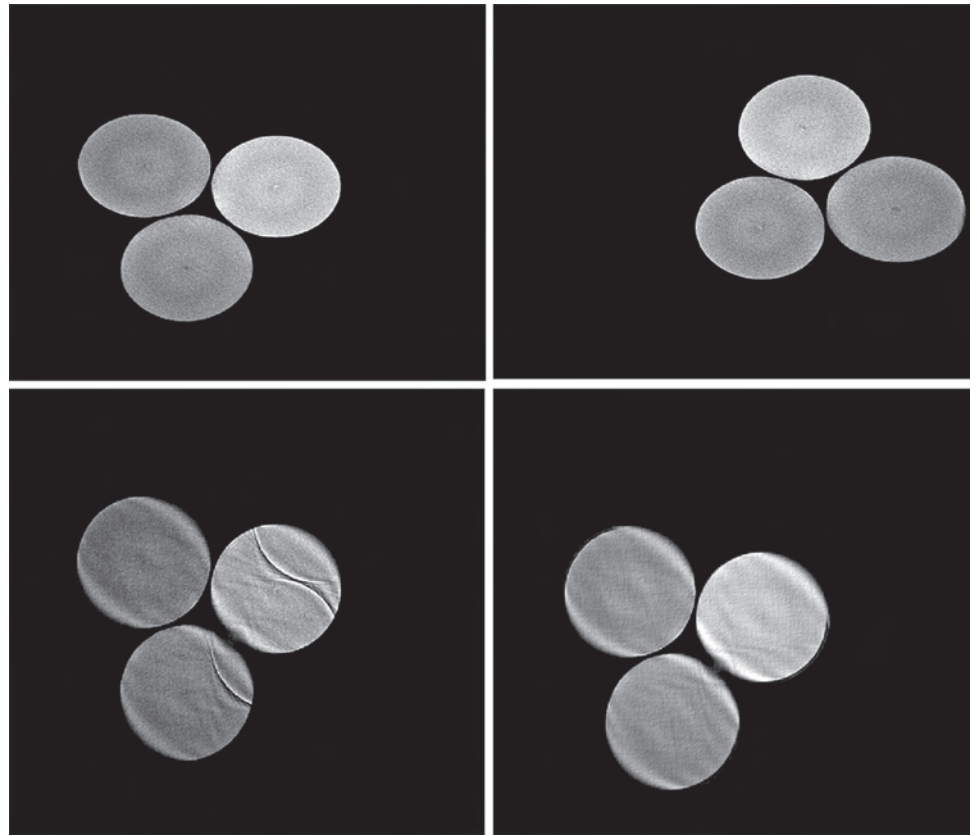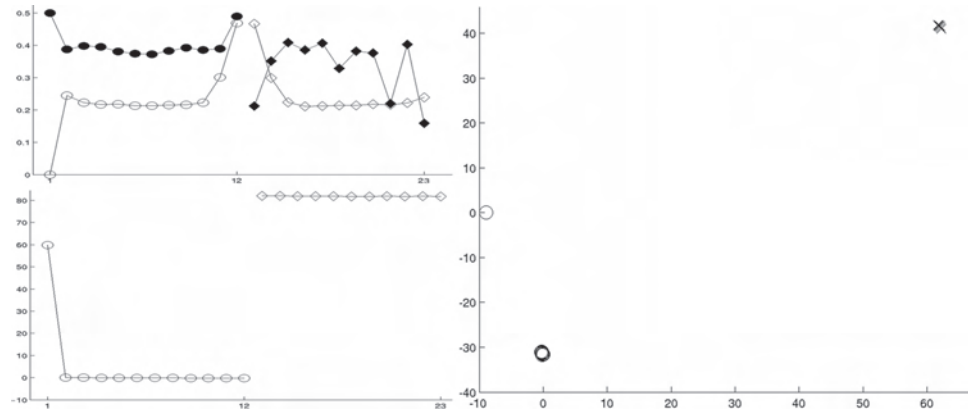

Figure 20. Top left: Average blade weights. Solid ovals indicate weights without motion correction; open ovals indicate weights with motion correction. Bottom left: Rotations in degrees per blade plotted against blade number. Right: Shifts in pixels plotted against blade number. Outlying shift is from blade 1.

$$\mathrm{F}[bl\,(R_\theta \mathbf{x})](\mathbf{k}) = [\mathrm{F}bl](R_\theta \mathbf{k}), \qquad (14)$$

where R_θ is a rotation matrix that rotates vectors $\mathbf{x}$ and $\mathbf{k}$ by angle θ, and bl represents a blade image. The goal is to use redundant data from the center of k-space to determine first how much in-plane rotation the object undergoes between blade acquisitions. For each blade, we have hundreds of low-frequency k-space samples from which we recover a single rotation value. This is done as described by Pipe (4), and rotation values are used during subsequent correction steps and the final regrid of all blades onto a single Cartesian lattice. Figures 19 and 20 show an extreme example in which a three-bottle phantom is manually rotated midway during image acquisition.

Translation Correction

Translation of an object results in a phase roll across its Fourier transform:

$$\mathrm{F}[bl\,(\mathbf{x} + \Delta\mathbf{x})](\mathbf{k}) = [\mathrm{F}bl](\mathbf{k})\,e^{-2\pi i \mathbf{k} \cdot \Delta\mathbf{x}}. \qquad (15)$$

This allows us to use the same redundant low-frequency data to estimate in-plane translation between blade acquisitions. This computation assumes that no rotation has occurred. Therefore, rotation correction must be applied before translation correction. Furthermore, tricks used during the rotation correction to minimize errors caused by T2 decay cannot be ap-
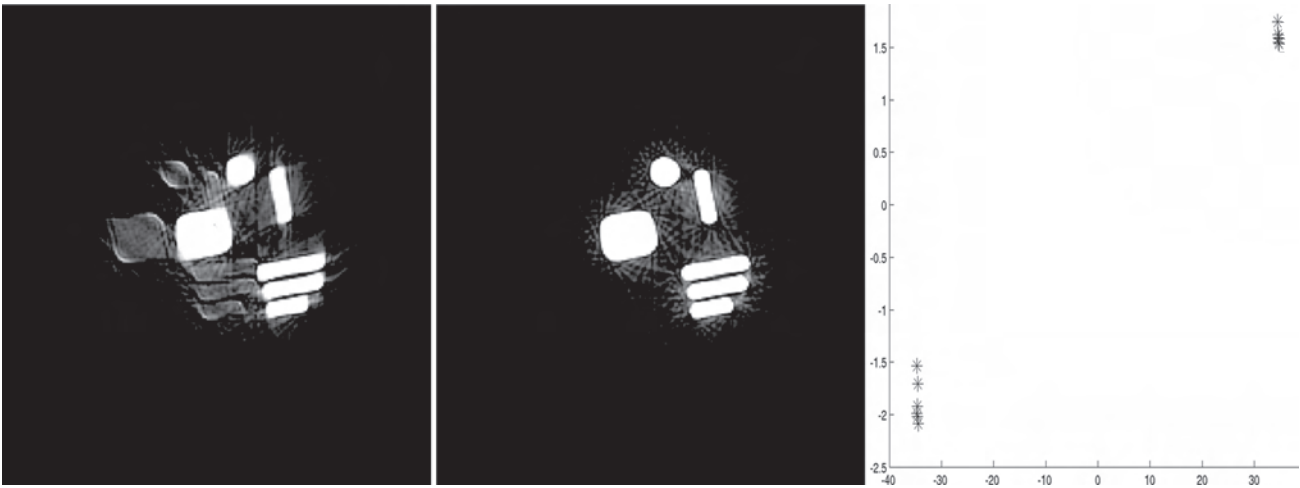
Figure 22. Image quality phantom was physically shifted midway through a 12-blade PROPELLER MR acquisition. Left: Data reconstructed without motion correction. Middle: Image reconstructed with motion correction. Right: Plots of the shifts computed for each blade (in pixels).
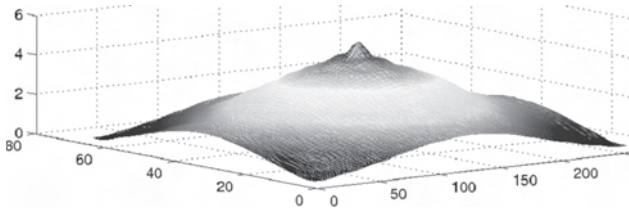

Figure 21. Magnitude of blade convolved against conjugate of reference blade. Notice that the function is reasonably smooth but does have a single well-defined peak.

plied directly to the translation computations, making shift estimates less accurate than rotation estimates. The method exploits Equation (3):

$$\mathrm{F}^{-1}[\mathrm{F}bl \ \mathrm{conj}(\mathrm{F}ref)](\mathbf{x}) = [bl * ref](x). \qquad (16)$$

In the ideal case, each blade is simply a translation of the reference blade. The convolution of a function with its complex conjugate achieves its maximum magnitude at the origin, and the convolution of the reference blade with a $\Delta\mathbf{x}$ translate of its complex conjugate achieves its maximum magnitude at $\Delta\mathbf{x}$.

The low-frequency k-space data for each blade are regridded onto the same Cartesian lattice points as the reference blade, by using rotation values corresponding to the blade orientation and the patient rotation estimates. Then the k-space data for each blade are multiplied pointwise by the complex conjugate of the reference blade. These are up-sampled and Fourier transformed into the image domain, computing the convolutions of each low-frequency blade image with the complex conjugate of the reference blade image. The peak magnitude of each convolution determines the blade's in-plane translation relative to the reference blade, as depicted in Figure 21. The estimates of

both patient rotation and translation are fed into subsequent reconstruction steps, the next being computing correlations of blade data:

$$
\begin{aligned}
\mathrm{F}^{-1}&[\mathrm{F}ref(\cdot + \Delta\mathbf{x})\mathrm{conj}(\mathrm{F}ref)](\mathbf{x}) \\
&= \mathrm{F}^{-1}[\mathrm{F}ref \, e^{-2\pi i \mathbf{k} \cdot \Delta\mathbf{x}} \, \mathrm{conj}(\mathrm{F}ref)](\mathbf{x}) \\
&= \mathrm{F}^{-1}[|\,\mathrm{F}ref\,|^2 \, e^{-2\pi i \mathbf{k} \cdot \Delta\mathbf{x}}](\mathbf{x}) \\
&= (\mathrm{F}^{-1}[|\,\mathrm{F}ref\,|^2] * \delta_{\Delta\mathbf{x}})(\mathbf{x}) \\
&= (\mathrm{F}^{-1}[|\,\mathrm{F}ref\,|^2])(\mathbf{x} - \Delta\mathbf{x}) \\
&= (ref * \mathrm{conj}(ref))(\mathbf{x} - \Delta\mathbf{x}).
\end{aligned}
\qquad (17)
$$

Images reconstructed with and without shift correction are shown in Figure 22.

Data Correlation

As clean and stable as the rotation and translation corrections may be in theory, they have one severe flaw in 2D PROPELLER imaging: Patient motion is rarely in plane. Patients typically make complicated motions spanning all three dimensions, and the motion correction steps described previously correct only for in-plane motion. Therefore, the lion's share of patient motion remains uncorrected and can corrupt final image quality simply because the data from different blades are not always consistent. Correlations of low-frequency k-space data are computed across blades, and blades with low correlation values are given low weight relative to blades that are well correlated. Severe out-of-plane patient motion during a particular blade's acquisition creates a low correlation value, so PROPELLER essentially "throws out" low-frequency data from that blade during final image reconstruction, as shown in Figure 23. The combination of in-plane motion correction with blade correlation and weighting results in substantially improved image quality, as shown in Figure 24.

Figure 24. Reconstructions of a single MR imaging data set collected from a healthy volunteer who rotated her head ±90° during acquisition. Top left: No correction. Top right: Correlation correction only. Bottom left: Motion correction only. Bottom right: Both motion and correlation correction.
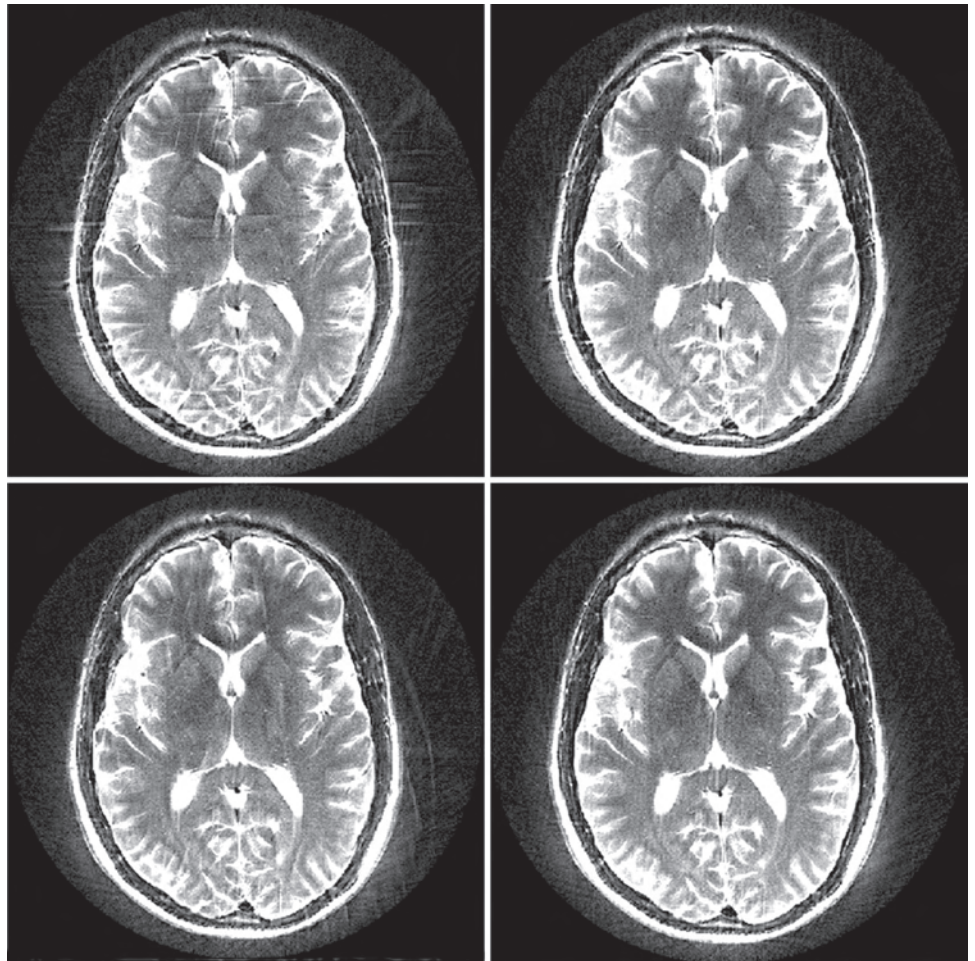
Density Correction

The density of points sampled within any blade is constant, so the density correction must handle only overlapping blades. In practice, PROPELLER's density correction at k-space point **k** combines this density correction with correlation values. These factors are combined into a weight for each data point in each blade. Phase-corrected k-space data are weighted by the combined density and correlation values prior to the final regridding. Both in-plane rotation and translation are accounted for during the final regridding, and the PROPELLER measurements are sampled onto a single Cartesian k-space lattice.

Final Grid

The last image preprocessing step is to grid the corrected blades onto a single Cartesian lattice. This is done by using a gridding method like those described earlier. Earlier correction steps (motion correction and correlation) required regridding the center of k-space and also used standard MR gridding. One advantage of PROPELLER is that it regrids from Cartesian lattices onto a Cartesian lattice. Therefore, "perfect" sinc interpolation can be used to up-sample each blade

Figure 23. Several blades are completely thrown out during the final gridding process, which fills in only the white region of k-space. Data were collected from a healthy volunteer who rotated her head ±90° during data acquisition.

(or blade center) before less-perfect regridding onto the (rotated) common Cartesian lattice, as sketched in Figure 25.

Gridding Deconvolution

As with any non-Cartesian acquisition scheme, the gridding convolution must be deconvolved to remove low-frequency shading across the image. Examples of pre- and postdeconvolution PROPELLER images are shown in Figure 5.
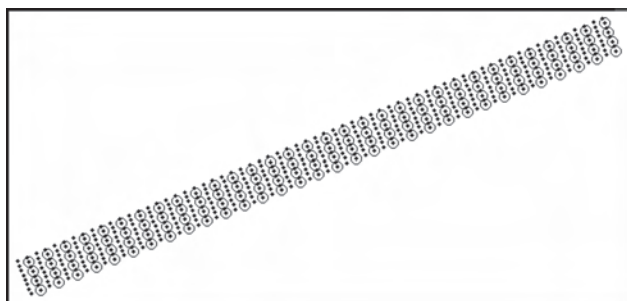
Figure 25. PROPELLER blades sample at points denoted by ○ and are up-sampled via sinc interpolation to the points denoted by ●.

Acknowledgments

References

1. Nam H, Patch SK. MRI with inhomogeneous background fields: pipe-dream or real possibility? In: Applied Science Laboratory technical note 04-01. Milwaukee, Wis: GE Healthcare, 2004 (available on request from the author).
2. Glover GH, Pelc NJ. Method for correcting image distortion due to gradient nonuniformity. U.S. patent 4,591,789. May 27, 1986.
3. Polzin JA, Kruger DG, Gurr DH, Brittain JH, Riederer SJ. Correction for gradient nonlinearity in continuously moving table MR imaging. Magn Reson Med 2004;52(1):181–187.
4. Pipe JG. Motion correction with PROPELLER MRI: application to head motion and free-breathing cardiac imaging. Magn Reson Med 1999;42(5):963–969.
5. Forbes KP, Pipe JG, Bird CR, Heiserman JE. PROPELLER MRI: clinical testing of a novel technique for quantification and compensation of head motion. J Magn Reson Imaging 2001;14(3):215–222.
6. Pipe JG, Farthing VG, Forbes KP. Multishot diffusion-weighted FSE using PROPELLER MRI. Magn Reson Med 2002;47(1):42–52. [Published correction appears in Magn Reson Med 2002;47(3):621.]
7. Arfanakis K, Tamhane AA, Pipe JG, Anastasio MA. k-Space undersampling in PROPELLER imaging. Magn Reson Med 2005;53(3):675–683.
8. Dym H, McKean HP. Fourier series and integrals. New York, NY: Academic Press, 1972.
9. Harris FJ. On the use of windows for harmonic analysis with the discrete Fourier transform. Proc IEEE 1978;66:66–67.
10. Jackson JI, Meyer CH, Nishimura DG, Macovski A. Selection of a convolution function for Fourier inversion using gridding. IEEE Trans Med Imaging 1991;10(3):473–478.
11. Rasche V, Proska R, Sinkus R, Bornert P, Eggers H. Resampling of data between arbitrary grids using convolution interpolation. IEEE Trans Med Imaging 1999;18(5):385–392.
12. Rosenfeld D. An optimal and efficient new gridding algorithm using singular value decomposition. Magn Reson Med 1998;40:14–23.
13. Sarty GE, Bennett R, Cox RW. Direct reconstruction of non-Cartesian k-space data using a nonuniform fast Fourier transform. Magn Reson Med 2001;45:908–915.
14. Van de Walle R, Barrett HH, Meyers KJ, et al. Reconstruction of MR images from data acquired on a general nonregular grid by pseudoinverse calculation. IEEE Trans Med Imaging 2000;19(12):1160–1167.
15. Carvalho JB, Patch SK. Reducing artifacts caused by interpolation between detector rows. In: Applied Science Laboratory technical note 01-04. Milwaukee, Wis: GE Healthcare, 2004 (available on request from the author).
16. Bernstein MA, King KF, Zhou XJ. Handbook of MRI pulse sequences. San Diego, Calif: Elsevier, 2004.